12-3-2018

Assessment of Different Methods for Shadow Detection in High-Resolution Optical Imagery and Evaluation of Shadow Impact on Calculation of NDVI and Evapotranspiration

Mahyar Aboutalebi
Utah State University, m.aboutalebi@aggiemail.usu.edu

Alfonso F. Torres-Rua
Utah State University, alfonso.torres@usu.edu

William P. Kustas
Hydrology and Remote Sensing Laboratory

Héctor Nieto
IRTA

Calvin Coopmans
Utah State University, coopmans@gmail.com

Mac McKee
Utah State University, mac.mckee@usu.edu

Recommended Citation

Aboutalebi, M., Torres-Rua, A.F., Kustas, W.P. et al. Irrig Sci (2019) 37: 407. https://doi.org/10.1007/s00271-018-0613-9

Irrigation Science manuscript No.
(will be inserted by the editor)

Assessment of different methods for shadow detection in high-resolution imagery and evaluation of shadows impact on calculation of NDVI, LAI, and evapotranspiration

Mahyar Aboutalebi · Alfonso F. Torres-Rua · William P. Kustas · Héctor Nieto · Calvin Coopmans · Mac McKee

Received: date / Accepted: date

Abstract There have been significant efforts recently in the application of high-resolution remote sensing imagery (i.e., sub-meter) captured by unmanned aerial vehicles (UAVs) for precision agricultural applications for high valued crops such as wine grapes. However, with such high resolution data shadows will appear in the imagery effectively reducing the reflectance and emission signal received by imaging sensors. To date, research that evaluates procedures to identify the occurrence of shadows at this geographic scale in imagery produced by UAVs is limited. In this study, the performance of four different shadow detection methods that have been used in satellite imagery were evaluated for high-resolution UAV imagery collected over a California vineyard during the Grape Remote sensing Atmospheric Profile and Evapotranspiration eXperiment (GRAPEX) field campaigns. The shadow detection methods were compared and the impacts of shadowed areas on vegetation indices such as the normalized difference vegetation index (NDVI) and leaf area index (LAI) are presented, as well as the impact on estimated evapotranspiration (ET) using a remote sensing-based energy balance model. The results obtained for shadow detection indicated that the supervised classification and index-based methods had better performance than two other methods.

Mahyar Aboutalebi
Ph.D. Student, Department of Civil and Environmental Engineering, Utah State University, 8200 Old Main Hill, Logan UT 84321, USA
E-mail: m.aboutalebi@aggiemail.usu.edu

Alfonso F. Torres-Rua
Assistant Professor, Civil and Environmental Engineering, Utah State University, 8200 Old Main Hill, Logan, UT 84322, USA E-mail: Alfonso.Torres@usu.edu

William P. Kustas
U. S. Department of Agriculture, Agricultural Research Service, Hydrology and Remote Sensing Laboratory, Beltsville, MD 20705, USA E-mail: Bill.Kustas@ars.usda.gov

Héctor Nieto
IRTA, Research and Technology Food and Agriculture, Efficient Use of Water in Agriculture Programme, Lleida 25003, SPAIN E-mail: hector.nieto@irta.cat

Calvin Coopmans
Research Professor, Department of Electrical and Computer Engineering, Utah State University, 8200 Old Main Hill, Logan, UT 84321 E-mail: coopmans@gmail.com

Mac McKee
Director, Utah Water Research Laboratory, Professor of Civil and Environmental Engineering, Utah State University, 8200 Old Main Hill, Logan, UT 84321, USA E-mail: Mac.Mckee@usu.edu

Furthermore, assessment of shadowed pixels in the vine canopy led to significant differences in the calculated NDVI, LAI and ET in areas affected by shadows in the high-resolution imagery.

Keywords shadow detection · supervised classification · unsupervised classification · index based method · vineyard · evapotranspiration · NDVI · LAI · ET

1 Introduction

Unmanned aerial vehicles (UAVs) used for remote sensing (RS) purposes have become a rapidly developing technology for acquiring high-resolution imagery of Earth surface objects and processes. However, as image resolution increases, new challenges emerge such as data transfer and storage, image processing, and detection and characterization of finer-scale features such as plant canopy glint, blurriness due to wind, and shadows. Although in some cases shadows might not be a significant issue, shadows affect reflectance and thermal emission not accounted in RS energy balance models, which in turn is likely to cause bias in determining plant water use and stress.

The use of UAVs for monitoring agricultural crop conditions has greatly expanded in recent years due to recent advances in high-resolution aerial image processing and sensor technology. These advances have extended the capability to measure crop conditions from a single field to multiple fields in a small time interval. The MIT Technology Review has listed Agricultural UAVs (or drones) as number one in 10 Breakthrough Technologies of 2014 ([18]). UAVs now offer sub-meter resolution remote sensing relevant to water management through optical and thermal imagery and evapotranspiration estimation advances. This UAV technology is now being applied to high-value crops such as orchards and vineyards to assess individual plant water use or evapotranspiration (ET) and stress (Ortega-Farias et al. 2016 ([23]); Nieto et al. this issue ([21])). This enhanced sensing capability can provide information of plant water use and symptoms for biotic/abiotic stresses at individual plant scale, a capability not achievable with commercial or NASA satellite data. Nevertheless, with incrementally finer resolution imagery being feasible, the effects of shadowed pixels become more pronounced. Therefore, neglecting the shadow impact on monitoring and detecting plant water use and stress and soil moisture status might well result in less reliable assessments for high-value crops.

Shadows appear when elevated objects, such as buildings or trees, occlude and block the direct light produced by a source of illumination. In some cases, information about shadows can provide additional clues about the geometric shape of the elevated object (Lillesand and Kiefer, 2000 [17]), the position of the source of light (Bethsda, 1997 [3]), and the height of the object (Sirmacek and Unsalan, 2008 [32]). In most cases, the appearance of shadows in an image acquired by RS complicates the detection of objects or areas of interest that are located under the shadowed area and thus reflect reduced radiance. The appearance of shadows in aerial imagery may also cause loss of valuable information about features, like shape, height, and color. Consequently, the darkening effect of shadows increases land cover classification error and causes problems for remote sensing studies, such as calculation of vegetation indices and change detection (Zhu and Woodcock, 2012 [36]). In addition, sun position changes lead to moving and changing shadow locations. As a result, shadow detection algorithms have received widespread attention, primarily with respect to the impacts of shadows on satellite RS data. Typical RS vegetation indices and outputs used in agriculture include NDVI, enhanced vegetation index (EVI), LAI (Carlson and Ripley, 1997 [6]), ET estimates (Nemani and Running, 1998 [20]), and land cover classification (Trout and Johnson, 2007 [34]), among others.

Multiple studies have been conducted to develop methods that detect shadows in images captured by satellites, and several shadow detection methods have been documented. These methods can be categorized into four groups: (a) unsupervised classification or clustering, (b) supervised classification that employ tools such as artificial neural networks (ANNs) or support vector machines (SVMs), (c) Index-based, and (d) physically-based methods.

(a) Unsupervised classification/clustering: Xia et al. (2009) [35] presented an unsupervised classification/clustering algorithm to detect shadows using the affinity propagation clustering technique in the Hue-Saturation-Intensity (HSI) color space. Shiting and Hong (2013) [30] presented a clustering-based shadow edge detection method using K-means clustering and punishment rules to modify false alarms. The experimental results revealed that the proposed method has a capability of producing a robust shadow edge mask.

(b)Supervised classification/object-based methods: Kumar et al. (2002) [14] proposed an object-based method to detect shadows using a color space other than RGB. Siala et al. (2004) [31] worked on a supervised classification method to detect moving shadows using support vectors in the color ratio space. Zhu and Woodcock (2012) [36] presented an object-based approach to detect shadows and clouds in Landsat imagery.

(c)Index-based methods: Scanlan et al. (1990) [29] reported a method to detect and remove shadows in images by partitioning the image into pixel blocks, calculating the mean of each block, and comparing it with the image median. Rosin and Ellis (1995) [26] worked on the impact of different thresholds on the detection of shadows in an index-based method. Choi and Bindschadler (2004) [7] presented an algorithm to detect clouds using normalized difference snow index (NDSI) to match plausible cloud shadow pixels based on solar position and Landsat7 images. Qiao et al. (2016) [24] used normalized difference water index (NDWI) and NDVI to separate shadow pixels from both water bodies and vegetation, and then applied a maximum likelihood classifier (MLC) and support vector machines (SVMs) to classify the shadow pixels. Kiran (2016) [13] converted an RGB color image to a grayscale image using the average of the three bands, and then used Otsus method to define a threshold for differentiating between shadow and non-shadow pixels. Finally, a histogram equalization method was applied to improve the contrast of the grayscale image.

(d)Physically-based methods: Sandnes (2010) [27] used the sun position and shadow length to approximately estimate the geolocation of the sensor. Huang and Chen (2009a) [11] presented a physical approach for detecting the shadows in video imagery and showed that the proposed method can effectively identify the shadows in three challenging video sequences. Also, Huang and Chen (2009b) [12] proposed a method for detecting a moving shadow using physical-based features. In this method, the physical-based color features are derived using a bi-illumination reflection model. More information about physically-based models can be found in Sanin et al. (2012) [28].

Ranson and Daughtry (1987) [25] and Leblon et al. (1996a)[15] concluded that NDVI estimates were highly sensitive to the shaded part of a forest canopy. Leblon et al. (1996b) [16] analyzed the mean sunlit and shadow reflectance spectra of shadows cast by a building and by conifers and hardwood trees on grass, bare soil, and asphalt using the visible and near-infrared bands. Their results indicated that reflectances of hardwood shadows were greater than those of conifers and buildings, except for shadow reflectance on bare soil. Moreover, the average NDVI and the atmospherically resistant vegetation index (ARVI) in sunlit areas could be lower or higher than in shaded areas depending on the surface type and shadow type. While the literature identifies several shadow detection approaches, few studies have focused on shadow detection for very high-resolution imagery captured by UAVs. Furthermore, limited work is available that demonstrates how shadows might affect the interpretation of the imagery in terms of vegetation indices, biophysical parameters and ET. Therefore, the objectives of this study were to characterize the advantages and disadvantages of a version of each shadow detection model group to high-resolution imagery captured by UAVs over complex canopy locations like vineyards, and consider the impacts of shaded pixels on NDVI, LAI, and ET estimations.

2 Material and Methods

2.1 Area of Study and UAV sensor descriptions

The high-resolution images for this study were collected by a small UAV over a vineyard located near Lodi, California (38.29 N 121.12 W), in Sacramento County as part of the GRAPEX project. The UAV was supplied and operated by the AggieAir Remote Sensing Group at the Utah Water Research Laboratory at Utah State University. The height of the vines and the row spacing are about 2 m and 3.35 m, respectively, and the orientation of the vine rows is predominantly East-West. Four sets of high-resolution imagery (20 cm or finer) were captured over the vineyard by a UAV in 2014, 2015, and 2016. These UAV flights were synchronized with Landsat satellite overpass dates and times. The data were used to evaluate the various shadow detection methods. The study area is shown in Figure 1, and information describing the images is summarized in Table 1. Also, details of the AggieAir aircraft, along with sensor payload, are shown in Figure 2. As described in Table 1, different optical cameras were used at every year (2014, 2015, 2016). These ranged from consumer-grade Canon S95 cameras to industrial type Lumenera monochrome cameras fitted with narrowband filters equivalent to Landsat 8 specifications. Following the imagery acquisition, a two-step image processing phase occurred including (1) radiometric calibration and (2) image mosaicking and orthorectification. In the first step, the digital images are converted into a measure of reflectance by estimating the ratio of reference images from pre- and post-flight reference panel readings. In the second step, all images were combined into one large mosaic and rectified into a local coordinate system (WGS84 N10) using the Agisoft software [1] and survey-grade GPS ground measurements. The output of this step is an orthorectified reflectance mosaic along with a digital elevation model (DEM). To determine true bare soil elevation a LIDAR digital terrain model (DTM) product for the same location, collected by the NASA G-LiHT project was used [19]. Further discussion about image pre-processing and sensor description is provided by Elarab et al. (2015) [8].

Table 1: Dates, times, cameras and optical filters used to capture images with the UAV

Date	UAV Flight Time (PDT)		Cameras and Optical Filters				
	Launch Time	Landing Time	RGB	NIR	Radiometric Response	MegaPixels	Spectral Response
9-Aug-14	11:30 AM	11:50 AM	Cannon S95	Cannon S95 modified (Manufacturer NIR block filter removed)	8-bit	10	RGB: typical CMOS NIR: extended CMOS NIR Kodak Wratten 750 nm LongPass filter
2-Jun-15	11:21 AM	12:06 PM	Lumenera Lt65R Color	Lumenera Lt65R Monochrome	14-bit	9	RGB: typical CMOS NIR: Schneider 820 nm LongPass filter
11-Jul-15	11:26 AM	12:00 PM	Lumenera Lt65R Color	Lumenera Lt65R Monochrome	14-bit	12	RGB: typical CMOS NIR: Schneider 820 nm LongPass filter
2-May-16	12:53 PM	1:17 PM	Lumenera Lt65R Mono	Lumenera Lt65R Mono	14-bit	12	RED: Landsat 8 Red Filter equivalent NIR: Landsat 8 NIR Filter equivalent

2.2 Shadow detection methods

Figure 3 provides a schematic overview of the four different shadow detection methods that were evaluated. For unsupervised k-means classification, the value of k (maximum number of classes) must be determined. When using supervised classification, the signature spectra for each of the categories must be previously identified. The index-based method required that an index be calculated using two or more spectral bands and the identification of a threshold value (digital number or reflectance). Because the shadowed pixels can be visually identified, the threshold value can be

Figure 1. Example of an aerial image of the study area captured by the AggieAir UAV on June 2015 (left), and NASA phenocam photographs for the same site (right, obtained on 24 March 2013 and 02 July 2 2013 during the growing season)

modified in a trial-and-error process. Application of the physically based model involved calculation of the sun position based on the central latitude and longitude of the imagery, together with the local time at the flight area. Since the case study is not a large area (<0.4 km^2) and the flight time is less than 20 minutes, we can assume that the sun position is constant for all pixels.

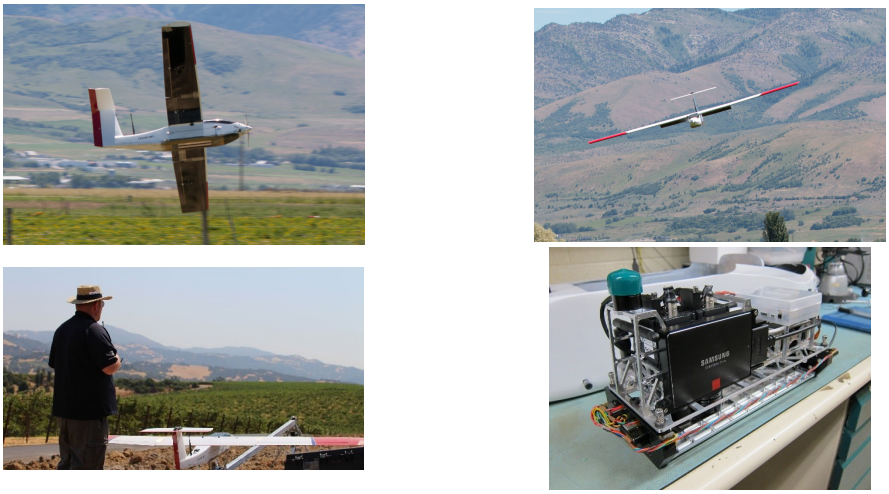

Figure 2. Photos of the AggieAir aircraft and its sensor payload

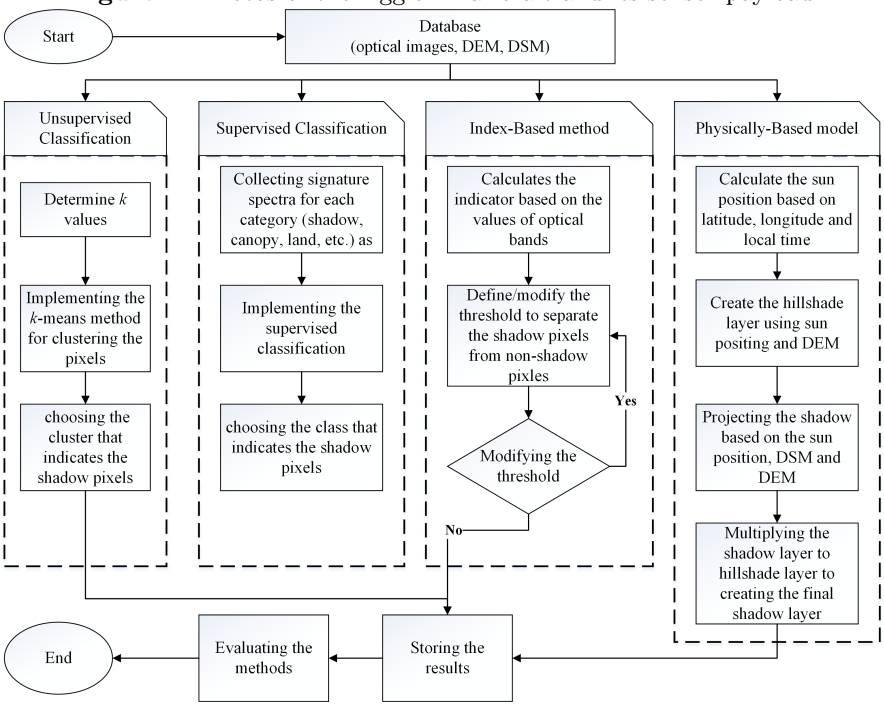

Figure 3. Flowchart illustrating the process of the study for evaluating the shadow detection methods using the very high resolution images captured by UAV

To statistically determine the impact of shadows over NDVI and LAI an ANOVA analysis was implemented. The ANOVA analysis compared shadowed and non-shadowed pixels over the canopy, and was applied to the best of the four shadow detection methods.

The first step to train the shadow models is to separate the canopy pixels from the ground pixels using DTM and DSM products for each image acquisition date. If the difference between DSM and DTM was greater than a threshold, that pixel could be considered as belonging to the

canopy vegetation; otherwise, it was assumed to be a pixel of bare ground/inter-row. This threshold filtered the canopy pixels in the images and its selection included a trial-and-error process.

Afterward, based on the filtering procedure and the evaluation of the shadow detection methods, the leaf canopy portions that were shaded or sunlit were extracted. From here, NDVI and LAI values were calculated and estimated separately for the shaded and sunlit portions of the canopy. This was done using Eq. 1 and Eq. 2 (proposed by Fuentes et al. 2014 [9] for vineyards). For both sets of NDVI and LAI pixels, the shadowed versus sunlit pixels were compared to each other in terms of histogram analysis and standard analysis of variance (ANOVA). The null hypothesis for the ANOVA test is that the average of the two populations are similar (e.g. the mean values of the shaded and sunlit NDVI pixels were equal). If the null hypothesis was rejected, a further comparison was performed on how the difference in shaded versus sunlit could affect NDVI, LAI and ET.

$$NDVI = \frac{R - NIR}{R + NIR} \tag{1}$$

$$LAI = 4.4 \times NDVI \tag{2}$$

3 Results and Discussion

3.1 Unsupervised classification (clustering)

Examples of the results of unsupervised classification (clustering) for shadow detection are illustrated in Figure 4 for the various flight dates over the study area. Five clusters were considered in applying the clustering method. These were generated based on the k-means method. The unsupervised classification toolbox of the ERDAS Imagine Software was used to execute the k-means algorithm. As shown in Figure 4, it is evident that most of the pixels that were assigned to Cluster 1 represent the pixels in shadows. Clusters 2 and 3 were mostly related to the sunlit vegetation canopy, and most of the pixels categorized into Clusters 4 and 5 were bare soil. In addition, some parts of the bare soil in the central part (dark pixels) of the 2015 images were classified as shadowed pixels (Cluster 1), which was not correct. Also, in the May 2016 image, some pixels classified in Cluster 5 (which were mostly bare soil pixels) overlapped with vegetation pixels. As shown in Table 1, only the red and NIR bands were used in 2016. This might have affected the performance of classification because it employed less information than was used for the imagery from the 2014 and 2015 UAV flights.

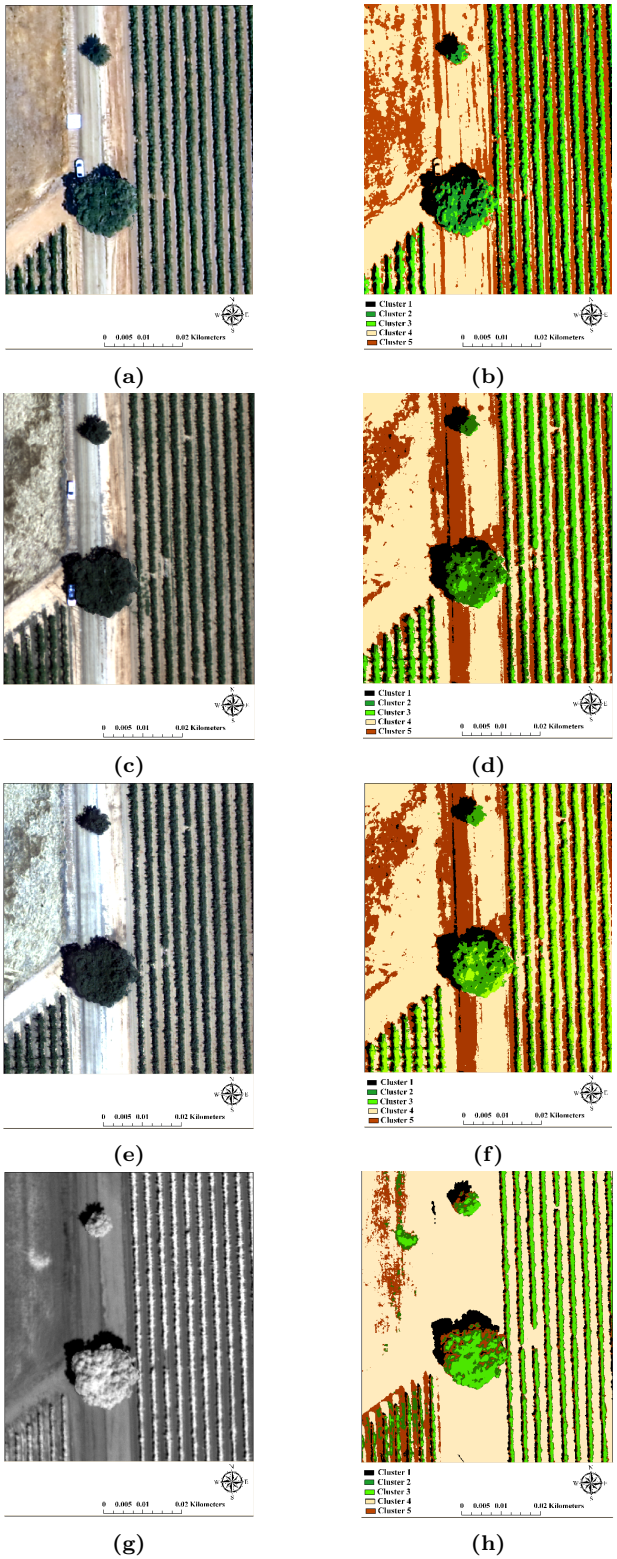

Figure 4. Original UAV image subset (left column) and unsupervised classification results (right column) from the vineyard imagery. (a) and (b) correspond to August 2014, (c) and (d) to June 2015, (e) (f) to July 2015 and (g) and (h) to May 2016. Black pixels on the right column represent shaded locations

3.2 Supervised Classification

The supervised classification results were obtained using the supervised classification of the ERDAS Imagine Software. Before running this model, a signature file was collected for each of the different targets (vegetation, shadow, bare soil) using the area of interest layers as the training areas and signature editor. Then each pixel was assigned to these discrete signature classes based on a maximum likelihood method. The results of the supervised classification method for shadow detection in images captured by the UAV in August 2014, June 2015, July 2015, and May 2016 are shown in Figure 5. From visual inspection, which is the customary approach used to evaluate the performance of different shadow detection methods (Tolt et al. [33], 2011), the performance of this classification for detecting shadows was better than that of the clustering approach, as can be seen by comparing the black pixels in the classified image to the pixels that are obviously in shadows in the true color image. In this method, however, selecting the targets and assigning them to classes is time-consuming.

3.3 Index or pixel-based methods

A MATLAB program was written for detecting shadowed pixels using the index-based method. In this program, the average of red and NIR bands was considered as a grayscale image. Then, based on a trial-and-error search, separate thresholds were applied to each band to separate shadowed from non-shadowed pixels. The results of the index-based method are illustrated in Figure 6. Again, from visual inspection of these figures, the performance of the index-based approach for detecting shadows is better than that of clustering, and somewhat better than that of the classification method. However, as discussed previously, to identify the shadowed pixels with this method, threshold values must be defined to separate the shadowed area from the original version of the image, which requires a trial-and-error approach and a visual histogram analysis.

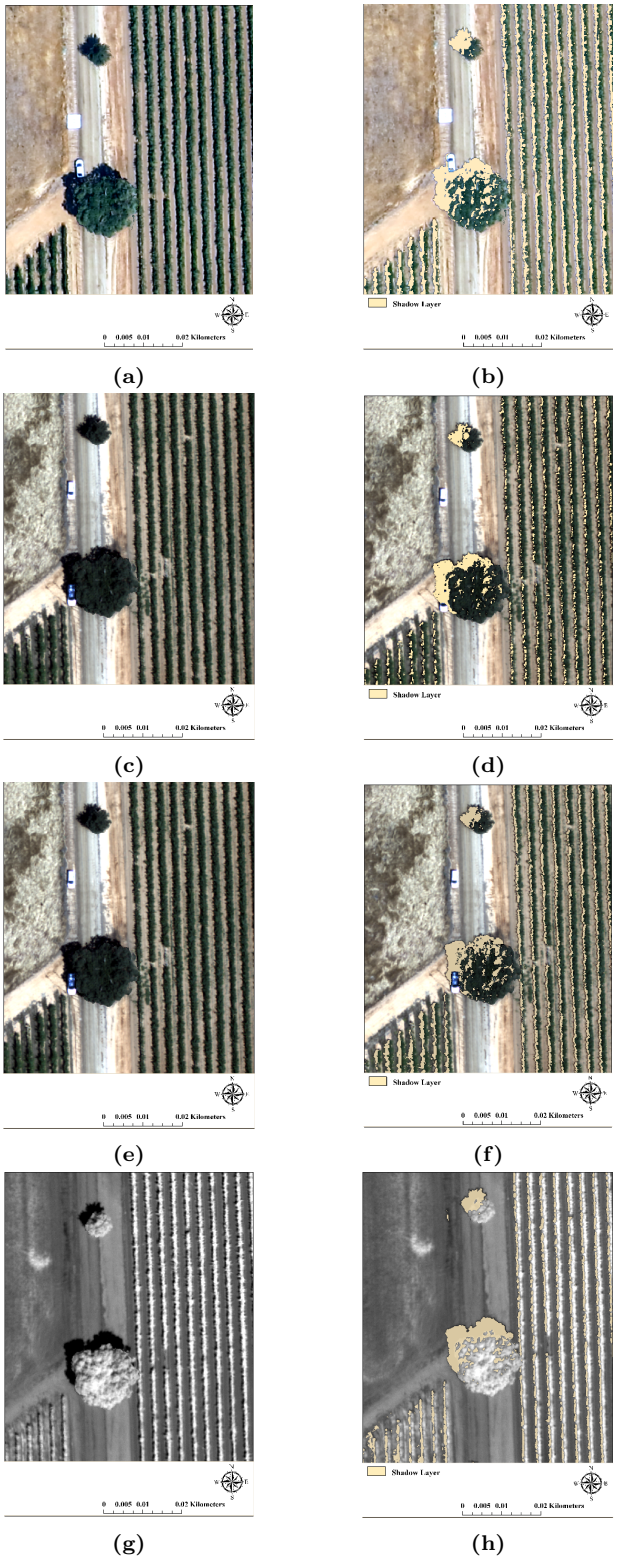

Figure 5. Original UAV image subset (left column) and supervised classification results (right column) from the vineyard imagery. (a) and (b) correspond to August 2014, (c) and (d) to June 2015, (e) (f) to July 2015 and (g) and (h) to May 2016. Beige pixels on the right column represent shaded locations

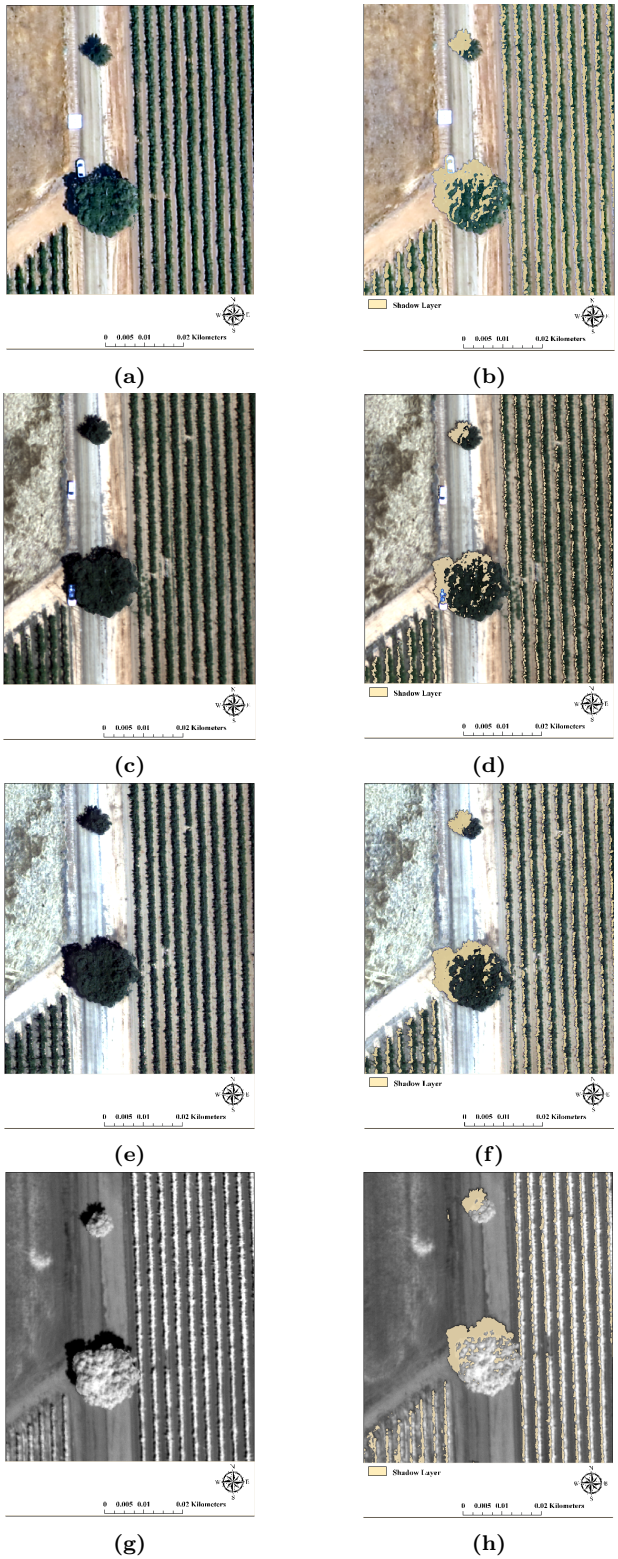

Figure 6. Original UAV image subset (left column) and index-based method classification results (right column) from the vineyard imagery. (a) and (b) correspond to August 2014, (c) and (d) to June 2015, (e) (f) to July 2015 and (g) and (h) to May 2016. Beige pixels on the right column represent shaded locations

3.4 Physically-based methods

The hillshade toolbox of ArcGIS was executed to project shadows according to the solar position, using DSM data. The results of this modeling are shown in Figure 7. These images show some errors within the leaf canopy when projecting the shadows using these tools. Although the ArcGIS hillshade toolbox is independent of the reflectance of each pixel, several factors can affect its accuracy. First, to execute the hillshade toolbox, we must define the solar position (azimuth and elevation). To determine the solar position, we need to know the latitude and longitude of the image, as well as the time that the image was captured by the UAV. Obviously, latitude and longitude are not fixed values over the entire image. Moreover, the duration of the flight is around 20 minutes. Therefore, the solar position is not consistent relative to all pixels, so we must estimate the solar position at around the average value for those parameters. Moreover, the accuracy of the hillshade projection critically depends upon the accuracy of the DSM. Similarly to the index-based method, separating the shadowed area from the image requires that we define a threshold. Thus, error sources for the ArcGIS hillshade method can be attributed to one or more of the following sources: (1) the accuracy of the DSM, (2) the threshold definition, (3) the use of an average value for the time at which the image was captured by the UAV, and (4) the use of an average value for latitude/longitude.

The Hillshade Toolbox in ArcGIS was executed to project shadows according to the solar time and position, and DSM data. The results of this modeling are shown in Figure 7. These images show some errors within the leaf canopy when projecting the shadows using these tools. Although the ArcGIS Hillshade Toolbox is independent of pixel reflectance, the main factor can affect its performance is related to DSM accuracy. Similarly to the index-based method, separating the shadowed area required a threshold selection. One advantage of using this method is the ability to generate the shadow layer in the absence of optical imagery. This is illustrated in Figure 8, wherein the diurnal shadow layer for a small part of the vineyard imagery captured by the UAV in July 2015 is simulated from 7:00 a.m. to 8:00 p.m.

3.5 Visual Assessment of Shadow Detection Model Performance

Figure 9 illustrates the shadow detection differences produced by the different classification methods over an area in the approximate center of the GRAPEX vineyard for imagery captured from the various UAV flights. The performance of the unsupervised and supervised classification approaches and the index-based method varies in this region of the image and serves to contrast their performance in detecting shadows.

From visual inspection of the imagery in Figure 9, the performance of these four classification methods in the center portion of the vineyard for the flights in August of 2014 (Figure 9.a, Figure 9.e, and Figure 9.i) and May of 2016 (Figure 9.d, Figure 9.h, and Figure 9.l) is acceptable. However, the threshold-based and supervised classification methods performed similarly to each other and much better than the unsupervised classification method (the yellow layer in Figure 9.f, Figure 9.g, Figure 9.j, and Figure 9.k, versus the black pixels in Figures 9.b and 9.c). In addition, the performance of the index-based method is superior to that of the supervised classification method in June 2015 (Figure 9.f versus Figure 9.j). In the flat area, the performance of physical-based method is better than others but within the leaf canopy it overestimates shadowed pixels (see Figure 7).

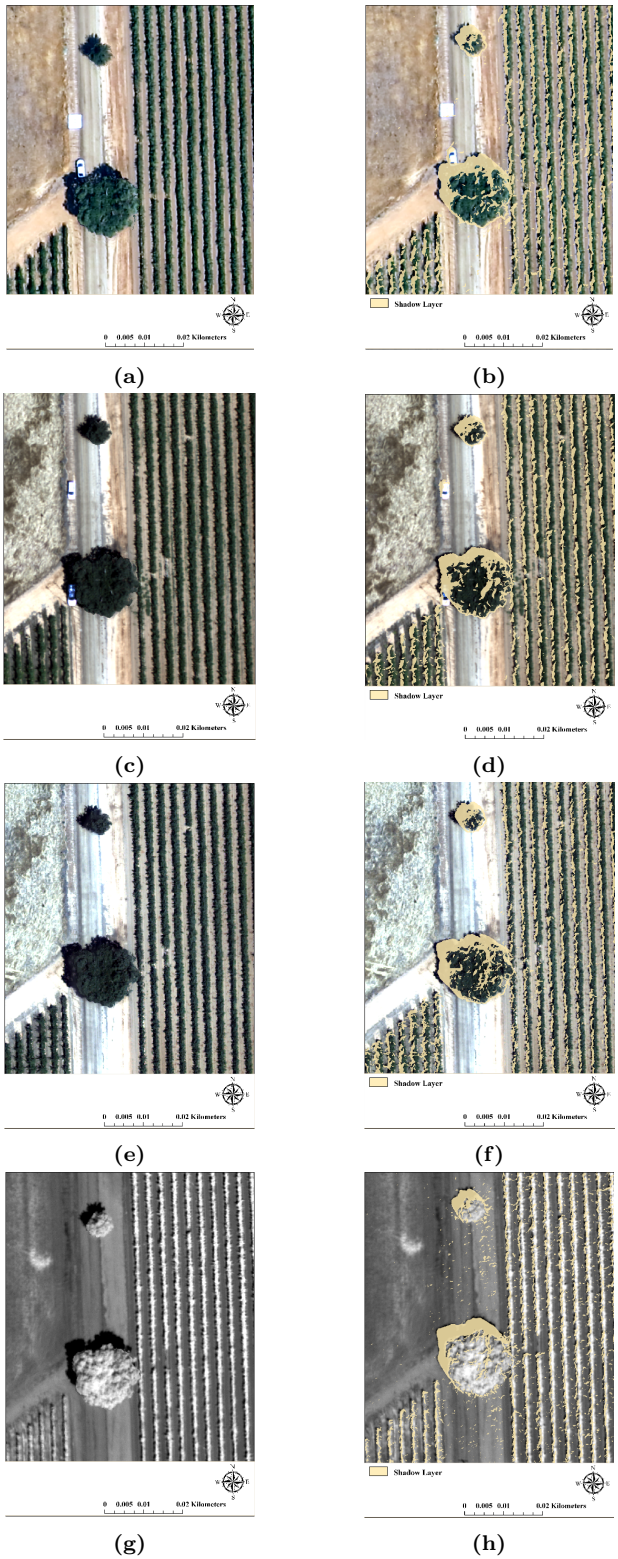

Figure 7. Original UAV image subset (left column) and physically method classification results (right column) from the vineyard imagery. (a) and (b) correspond to August 2014, (c) and (d) to June 2015, (e) (f) to July 2015 and (g) and (h) to May 2016. Beige pixels on the right column represent shaded locations

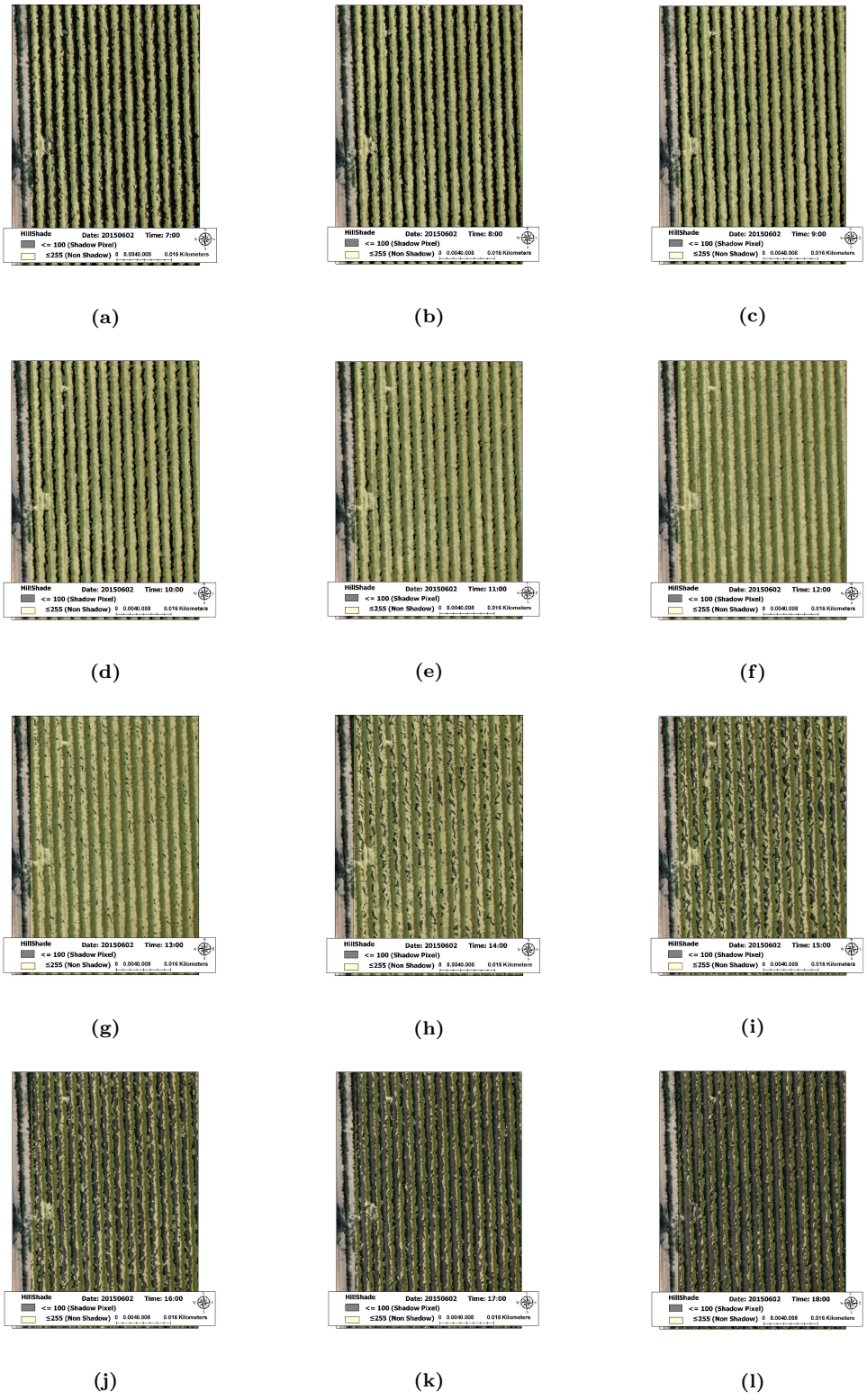

(a) **(b)** **(c)**

(d) **(e)** **(f)**

(g) **(h)** **(i)**

(j) **(k)** **(l)**

Figure 8. Simulated diurnal shadow pattern shown hourly, from 7:00 a.m. to 8:00 p.m., using the physically based model and shown on the background image captured by the UAV on July 2015 around 11:45 am PST. shadow layer for 7:00 a.m. (a), 8:00 a.m. (b), 9:00 a.m. (c), 10:00 a.m. (d), 11:00 a.m. (e), 12:00 a.m. (f), 1:00 p.m. (g), 2:00 p.m. (h), 3:00 p.m. (i), 4:00 p.m. (j), 5:00 p.m. (k), 6:00 p.m. (l). Dark areas indicate shadow locations.

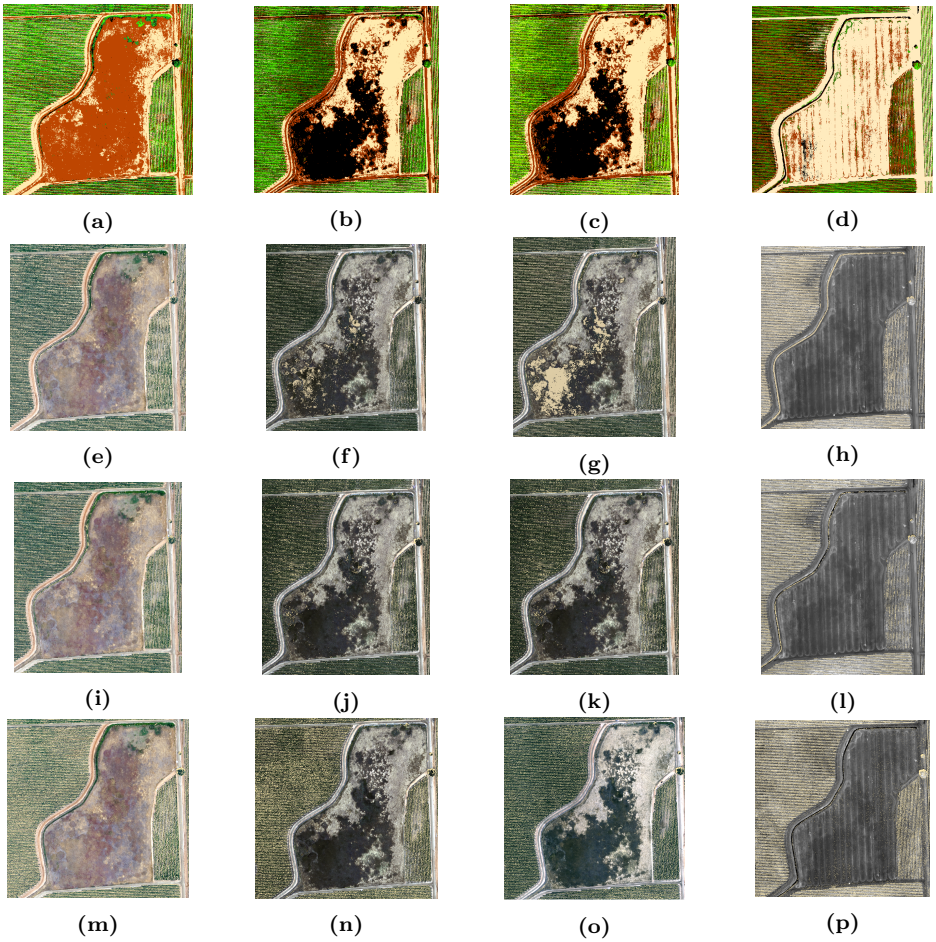

Figure 9. Classification maps of the center portion of the vineyard using unsupervised classification for August of 2014 (a), June of 2015 (b), July of 2015 (c), and May of 2016 (d); using supervised classification for for August of 2014 (e), June of 2015 (f), July of 2015 (g), and May of 2016 (h); using the index-based method for for August of 2014 (i), June of 2015 (j), July 2015 (k), and May of 2016 (l); using physical-based method for for August of 2014 (m), June of 2015 (n), July of 2015 (o), and May of 2016 (p)

3.6 Statistical Assessment of Shadow Detection Method Performance

Since shadow detection is a classification task, one approach for evaluating the accuracy of classification methods is the use the confusion matrix and report the correctness metric (or users accuracy described in Congalton, 1991 [4]) shown in (Eq. 3). To create a confusion matrix, the images on the left column of Fig 5 were manually separated into two categories: (1) shadowed and (2) non-shadowed area. Afterward, each class in the manually extracted method was compared to the corresponding class in each of the classification methods. Ultimately, the correctness metric (Eq. 3) was calculated based on the confusion matrix. The results of the confusion matrix, along with the correctness metric, are shown in Table 2. According to the correctness metric, the accuracy of the index-based (∼94%) method and the supervised (∼92%) method is higher than for the unsupervised (∼83%) method and the physically-based (∼87%) method. These results confirmed the visual assessment performed in the previous subsection.

$$correctness_{metric} = \frac{TP}{TP + FN} \tag{3}$$

in which TP = the numbers of shadow pixels identified correctly, and FN = the numbers of shadow pixels categorized into non-shadow class.

Table 2: Assessment accuracy between different methods and manually extracted method for a small part of the study of area

Date of Flight	Item	Method	Unsupervised		Supervised		Index-Based		Physically-Based	
			Method		Method		Method		Method	
		Classes	Shadow	Non-Shadow	Shadow	Non-Shadow	Shadow	Non-Shadow	Shadow	Non-Shadow
2014, August	Manually Extracted	Shadow	27039	6742	31292	2489	32683	1098	29455	4326
		Non-Shadow	20485	170695	8433	182747	5608	185572	10598	180582
		Total	47524	177437	39725	185236	38291	186670	40053	184908
	Assessment Accuracy (Correctness Metric)		80.57%		93.47%		96.75%		87.19%	
2015, June	Manually Extracted	Shadow	19038	3917	21038	1917	21393	1562	20084	2871
		Non-Shadow	2566	199440	2109	199897	1192	200814	2456	199550
		Total	21604	203357	23147	201814	22585	202376	22540	202421
	Assessment Accuracy (Correctness Metric)		82.94%		91.65%		93.20%		87.49%	
2015, July	Manually Extracted	Shadow	11845	2416	13030	1231	13320	941	12497	1764
		Non-Shadow	3454	207246	2561	208139	1459	209241	2964	207736
		Total	15299	209662	15591	209370	14779	210182	15461	209500
	Assessment Accuracy (Correctness Metric)		83.06%		91.37%		93.40%		87.63%	
2016, May	Manually Extracted	Shadow	18301	3459	19668	2092	20268	1492	18796	2964
		Non-Shadow	5697	197504	3294	199907	2314	200887	4198	199003
		Total	23998	200963	22962	201999	22582	202379	22994	201967
	Assessment Accuracy (Correctness Metric)		84.10%		90.39%		93.14%		86.38%	

3.7 The impacts of shadows on NDVI, LAI and ET

The results of evaluating NDVI and LAI in both the sunlit and shaded areas of the vineyard leaf canopy are presented here. As discussed in the Methodology Section, assessing the impact of shadows on NDVI, and LAI involved extracting two groups of pixels, sunlit and shaded, using two steps. The first step separates the vine canopy pixels from the ground surface and inter-row areas using DTM and DSM data. The second step is the results from the index-based shadow detection method. To test the equality of these two groups, ANOVA was used on the NDVI and LAI data from Eq. 4 and Eq. 5. Since LAI and NDVI are correlated to each other based on the linear equation, only the results of ANOVA for LAI is presented in Table 3. The null hypothesis in the ANOVA is

that mean in both groups (sunlit pixels and shaded pixels) are equal. The results of ANOVA for all images are presented in Table 3.

$$H_0 : \mu_1 = \mu_2 \tag{4}$$

$$H_1 : \mu_1 \neq \mu_2 \tag{5}$$

in which H_0 and H_1 are the null and alternative hypotheses, respectively, and μ_1 and μ_2 are the mean of the two groups (in this study, NDVI or LAI on, respectively, the sunlit and shaded leaf canopy).

Table 3: ANOVA results for LAI for the different flights acquired between 2014 and 2016

Flight Date	Source of Variation	SS	df	MS	F (observed)	P-value	F (critical)
August 2014	Groups	0.35	1	0.35	4.37	0.03	3.86
	Error	98.80	1222	0.08			
	Total	99.15	1223				
June 2015	Groups	4.00	1	4.00	31.04	0	3.86
	Error	125.36	972	0.12			
	Total	129.37	973				
July 2015	Groups	0.03	1	0.03	8.08	0	3.86
	Error	5.36	1222	0.004			
	Total	5.39	1223				
May 2016	Groups	3.21	1	3.21	20.5	0	3.75
	Error	152.77	974	0.15			
	Total	155.98	975				

As shown in Table 3, the F-statistic (observed value) is greater than the critical value for F. Therefore, the null hypothesis is rejected for all images. This means that there is a statistically significant difference between the values of NDVI and LAI, respectively, for the shadowed and non-shadowed pixels within the vine canopy. The histograms shown in Figure 10 further illustrate the difference in the distribution of NDVI and LAI values for the UAV flights conducted in 2014, 2015, and 2016.

A close examination of the distribution range of the shadowed pixels as presented in Figure 10 indicates that it is smaller than that of sunlit pixels. In addition, the average values of NDVI and LAI in the sunlit pixels is higher than those in the shadowed pixels. This means that ignoring the effect of shadows on NDVI and LAI estimations can lead to biased results and conclusions when using these variables. The LAI is a critical input to land surface models for ET estimation and hence shadow effects over this biophysical variable will cause error if the models ignore or fail to compensate for the bias on the LAI estimates. For example, in the two-source energy balance (TSEB) model developed Norman et al. (1995) [22], the radiometric temperature sensed at the satellite is partitioned into canopy temperature (T_c) and soil temperature (T_s) components using Eq. 6.

$$T_R = [f_c(\phi)T_c^4 + (1 - f_c(\phi))T_s^4]^{0.25} \tag{6}$$

in which $f_c(\phi)$ is the vegetation cover fraction as the thermal sensor with view angle ϕ and can be calculated using a Eq. 7 proposed by Campbell and Norman (1998) [5].

$$f_c(\phi) = 1 - \exp\frac{-0.5\Omega(\phi)LAI}{\cos\phi} \tag{7}$$

in which Ω is a clumping factor and LAI can be estimated using an empirical NDVI-LAI relation (Anderson et al. 2004 [2]). In the case of vineyards, a more sophisticated radiation and wind extinction algorithm in the TSEB model developed by Nieto et al. 2017 (this issue) requires several additional inputs including LAI. To evaluate the impact of shadows on energy balance components, TSEB was applied considering two scenarios (with and without masking shadows), one in which canopy parameters (LAI, canopy width) are estimated from the original VNIR images, and a second in which the canopy parameters are estimated with the image after masking out the shadows. Moreover, in order to preserve the assumptions in TSEB related to turbulent transport, TSEB was run by aggregating the UAV imagery to 3.6m. The impact on the magnitude of the energy balance components and their distribution is illustrated in Figures 11-14 for the UAV image of August 2014. These figures show the spatial absolute differences of fluxes as well as histogram and relative cumulative frequency of fluxes for both scenarios (with and without masking shadows). In the histograms, there is a clear shift for soil heat flux (G) indicating that the peak is moved to the right when shadows are involved. Since the NDVI-derived LAI present higher values when shaded pixels are removed, LAI yields larger values and therefore net radiation (Rn) reaching the ground is decreased. As G is a ratio of Rn at the soil surface in TSEB led to an increment of G when shadows are not removed. In contrast, for considering shadow scenario, the peak of sensible heat flux (H) and Rn are shifted to the left and those fluxes are smaller. With increasing G and decreasing Rn accounting for shadows, then the available energy (Rn-G) is decreasing. As shown in Figure 13, H decreased slightly due to slight changes in the soil temperature and canopy temperature values derived from a lower LAI in involving shadows scenario. For the latent heat flux (LE) considering the shadows results in a slight shift in the LE distribution to larger values and a greater number of LE values at the centroid of the distribution.

Also, an additional evaluation of the shadow impact on crop water stress using Bowen Ratio was performed as shown in Figures 15 and 16. These figures indicate that ignoring shadows led to larger water stress areas particularly in the southern section of the field. Moreover, the histograms show there are some differences (approximately 6%) in the water stress index calculated by involving versus ignoring the shadows. Still, additional analysis using eddy covariance measurements can help to further refine the differences found among energy balance components, Bowen Ratio and ET.

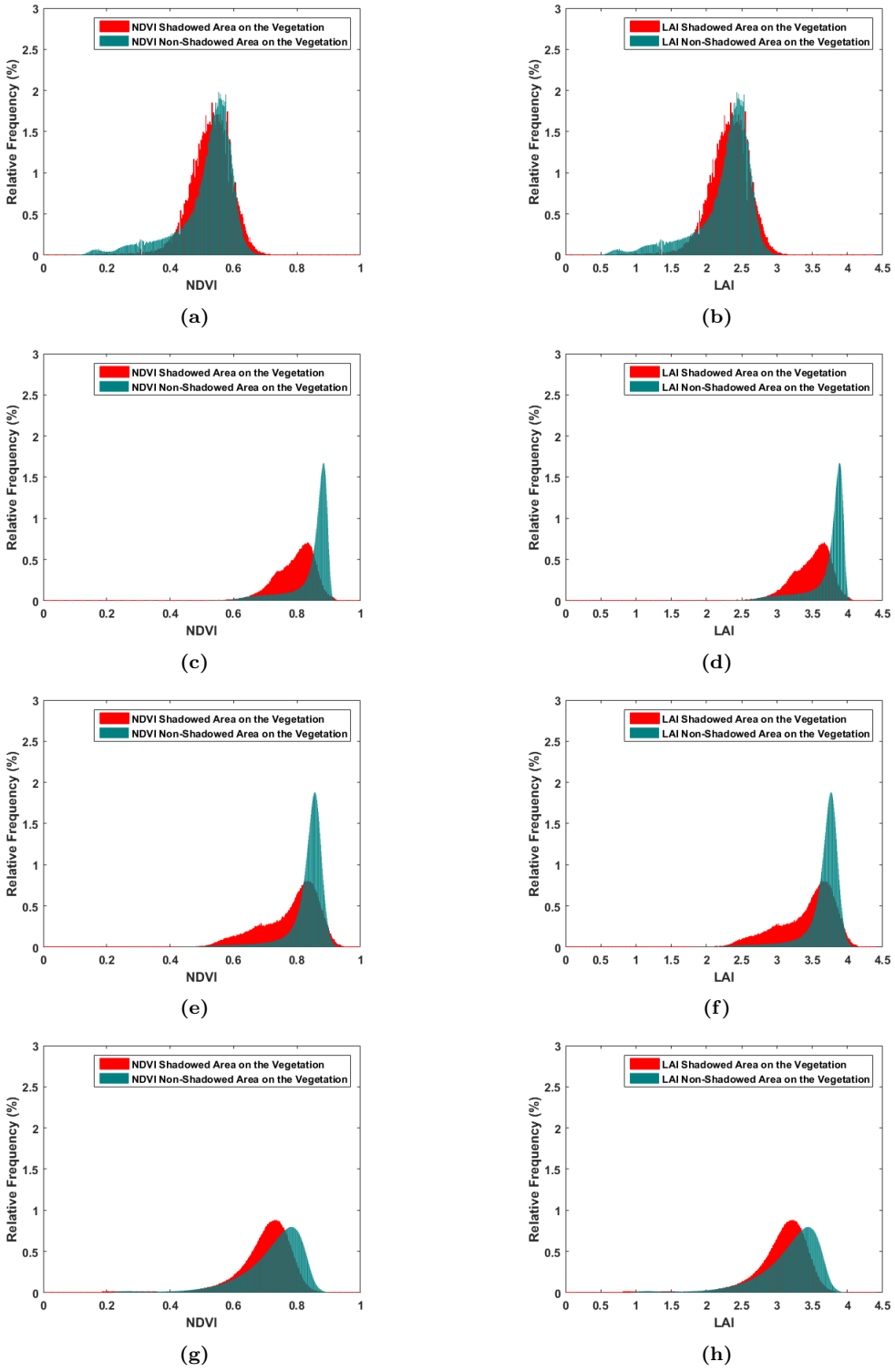

Figure 10. The NDVI histograms for the shadowed and sunlit pixels (a), and LAI histograms for the shadowed pixels and sunlit pixels (b) for the August 2014 imagery; the NDVI histograms for the shadowed and sunlit pixels (c), and LAI histograms for the shadowed pixels and sunlit pixels (d) for the June 2015 imagery; the NDVI histograms for the shadowed and sunlit pixels (e), and LAI histograms for the shadowed pixels and sunlit pixels (f) for the July 2015 imagery; the NDVI histograms for the shadowed and sunlit pixels (g), and LAI histograms for the shadowed pixels and sunlit pixels (h) for the May 2016 imagery.

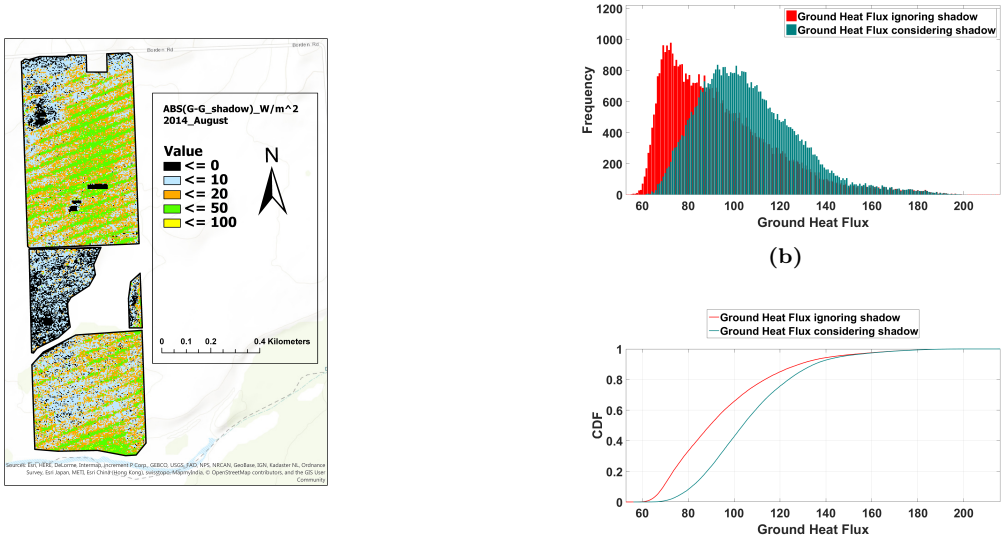

(a) (b) (c)

Figure 11. Flight August, 2014; the spatial absolute differences of soil heat flux considering shadows and ignoring shadows (a), histogram of soil heat flux considering/ignoring shadows (b), CDF of soil heat flux considering/ignoring shadows (c)

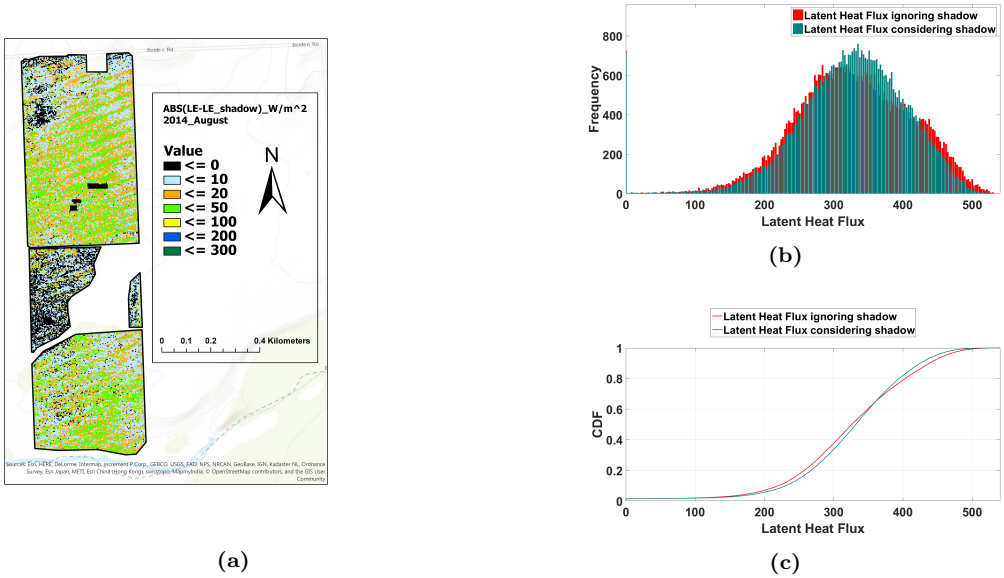

(a) (b) (c)

Figure 12. Flight August, 2014; the spatial absolute differences of latent heat flux considering shadows and ignoring shadows (a), histogram of latent heat flux considering/ignoring shadows (b), CDF of latent heat flux considering/ignoring shadows (c)

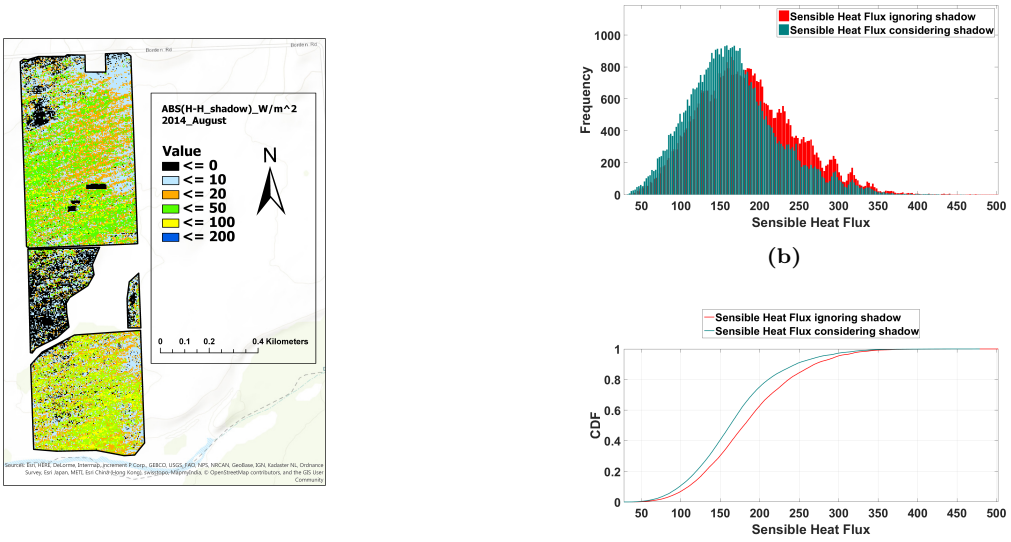

Figure 13. Flight August, 2014; the spatial absolute differences of sensible heat flux considering shadows and ignoring shadows (a), histogram of sensible heat flux considering/ignoring shadows (b), CDF of sensible heat flux considering/ignoring shadows (c)

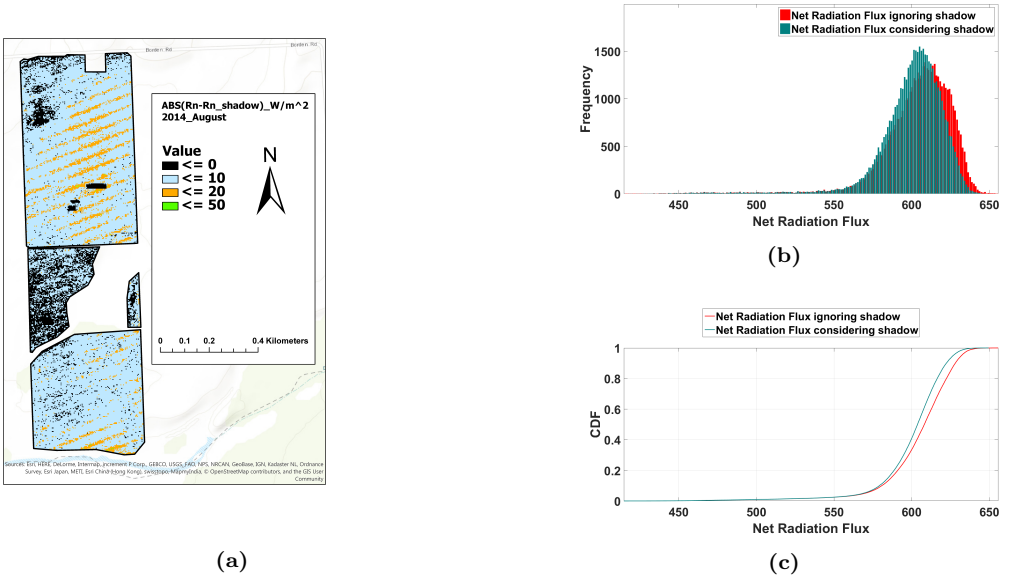

Figure 14. Flight August, 2014; the spatial absolute differences of net radiation flux considering shadows and ignoring shadows (a), histogram of net radiation considering/ignoring shadows (b), CDF of net radiation flux considering/ignoring shadows (c)

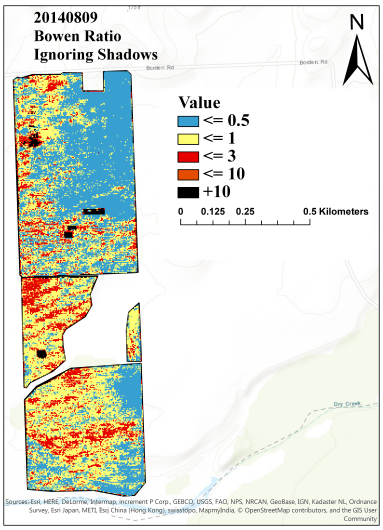

(a)]

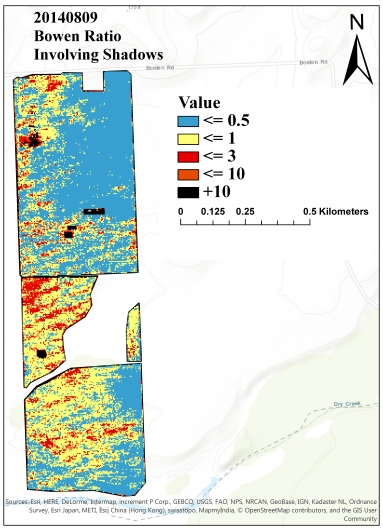

(b)

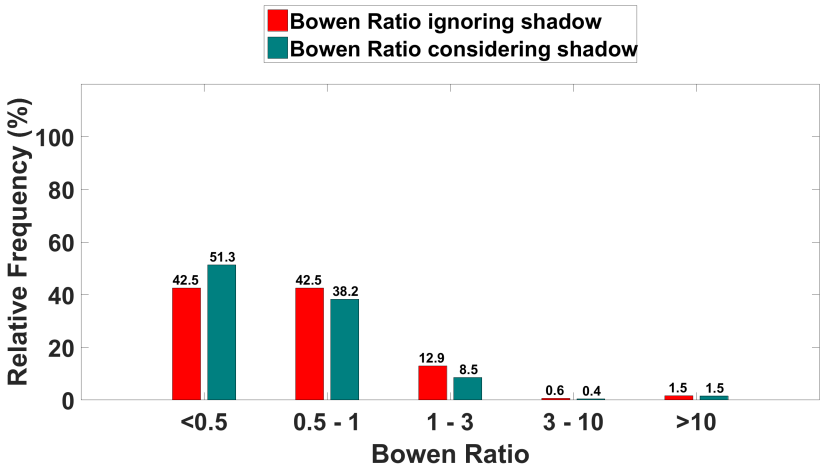

(c)

Figure 15. Flight August, 2014; Bowen Ratio ignoring shadows (a), Bowen Ratio involving shadows (b), Histogram of Bowen Ratio ignoring/involving shadows (c).

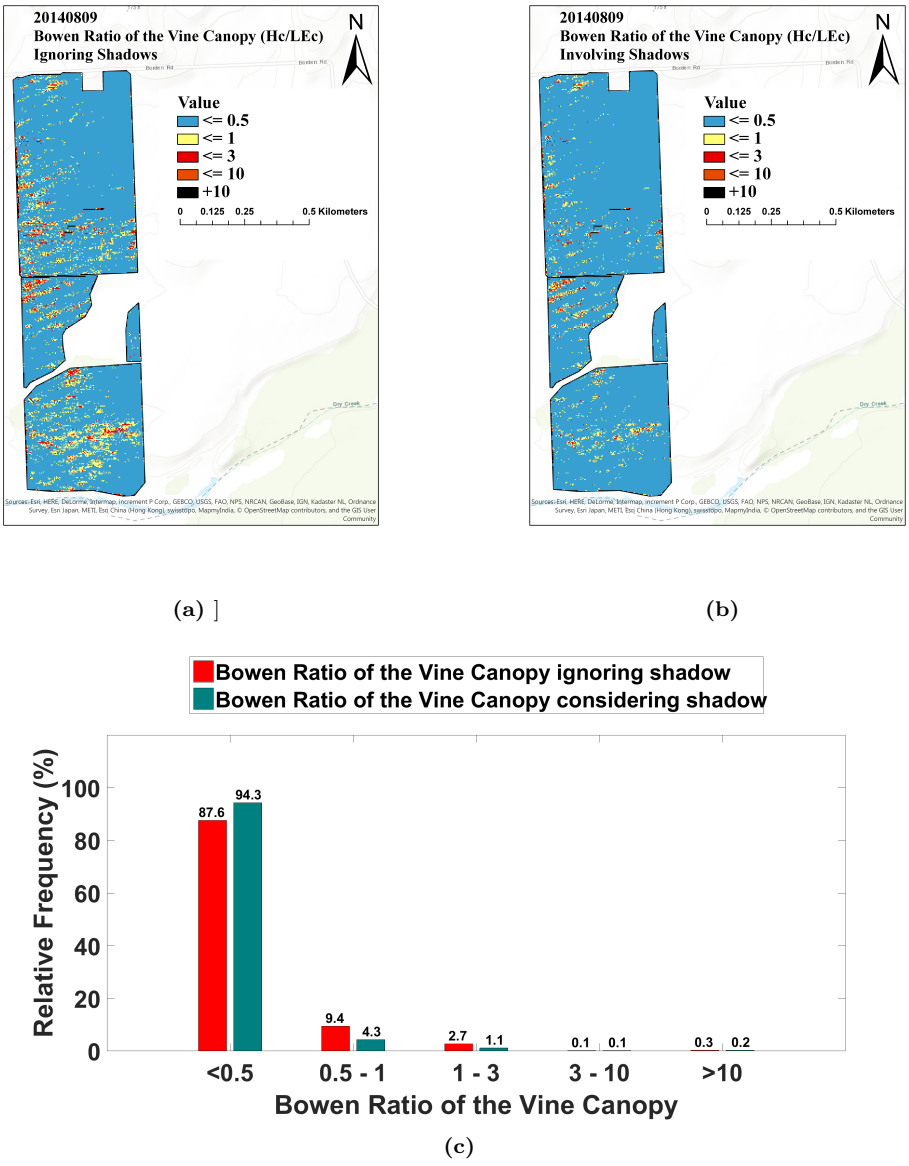

Figure 16. Flight August, 2014; (a) Bowen Ratio of the vine canopy ignoring shadows, (b) Bowen Ratio of the vine canopy involving shadows, (c) Histogram of Bowen Ratio of the vine canopy ignoring/involving shadows.

The ANOVA was used to test whether there was a significant difference in the fluxes computed by TSEB when accounting versus ignoring shadows. The results of ANOVA for those fluxes are presented in Table 4 to 7. The ANOVA results indicate that there is a statistically significant difference in ignoring versus accounting for shading for G and for most of the flights for Rn. However, in only half the flights does the ANOVA indicate accounting for shadows makes a difference in the output of H (August, 2014 and June, 2015 flights) and in only one of the flights for LE

(May, 2016 flight). Although ANOVA doesn't indicate a significant difference for LE in 2014 and 2015 flights, it is important to note that ANOVA is used for testing the equality of the means of the distributions and consequently doesn't evaluate differences in the flux distributions between ignoring and accounting for shadows. For this reason, the spatial differences in the fluxes shown in Figures 11 - 14 in order to have an idea where in certain areas of the vineyard significant discrepancies can exist.

Table 4: ANOVA results for G flux for the different flights acquired between 2014 and 2016

Parameter	Source of Variation	SS	df	MS	F (observed)	P-value	F (critical)
August 2014 (G)	Groups	33484.5	1	33484.5	60.73	0	3.84
	Error	550286.6	998	551.4			
	Total	583771.1	999				
June 2015 (G)	Groups	7064.16	1	7064.16	4.01	0.0456	3.84
	Error	1787208.13	1014	1762.53			
	Total	1794272.25	1015				
July 2015 (G)	Groups	24355.7	1	24355.7	23.14	0	3.84
	Error	1063052.4	1010	1052.5			
	Total	1087408	1011				
May 2016 (G)	Groups	13811.9	1	13811.9	13.26	0.0003	3.84
	Error	1035735.6	994	1042			
	Total	1049547.5	995				

Table 5: ANOVA results for H flux for the different flights acquired between 2014 and 2016

Parameter	Source of Variation	SS	df	MS	F (observed)	P-value	F (critical)
August 2014 (H)	Groups	77736.5	1	77736.5	21.82	0	3.84
	Error	3519222.3	988	3562			
	Total	3596958.8	989				
June 2015 (H)	Groups	58627.9	1	58627.9	3.96	0.0467	3.84
	Error	14544242	984	14781.5			
	Total	14602869	985				
July 2015 (H)	Groups	26698.01	1	26698	1.33	0.2499	3.84
	Error	20223718	1004	20143.1			
	Total	20250416	1005				
May 2016 (H)	Groups	2157.86	1	2157.86	0.82	0.3656	3.84
	Error	2602439	988	2634.05			
	Total	2604596.75	989				

4 Conclusions

Shadows are an unavoidable component of high-resolution RS imagery. If ignored, they can cause bias in products derived from RS data that are intended for monitoring plant and soil conditions. In this study, four different shadow detection methods were applied to very-high-resolution images captured by a UAV at various times over a GRAPEX vineyard and evaluated for accuracy.

Table 6: ANOVA results for LE flux for the different flights acquired between 2014 and 2016

Parameter	Source of Variation	SS	df	MS	F (observed)	P-value	F (critical)
August 2014 (LE)	Groups	2280.2	1	2280.2	0.38	0	3.84
	Error	6000867	998	6012.89			
	Total	6003147	999				
June 2015 (LE)	Groups	14609.2	1	14609.2	0.59	0.4436	3.84
	Error	24472706	984	24870.6			
	Total	24487316	985				
July 2015 (LE)	Groups	4889.28	1	4889.3	0.16	0.6854	3.84
	Error	29661146	996	29780.3			
	Total	29666036	997				
May 2016 (LE)	Groups	11763.3	1	11763.3	4.07	0.0439	3.84
	Error	2889741.5	1000	2889.7			
	Total	2901504.2	1001				

Table 7: ANOVA results for Rn flux for the different flights acquired between 2014 and 2016

Parameter	Source of Variation	SS	df	MS	F (observed)	P-value	F (critical)
August 2014 (Rn)	Groups	4022.5	1	4022.48	8.13	0.0044	3.84
	Error	482734.6	976	494.61			
	Total	486757.1	977				
June 2015 (Rn)	Groups	745.291	1	745.29	0.63	0.4261	3.84
	Error	1140210.55	970	1175.47			
	Total	1140955.5	971				
July 2015 (Rn)	Groups	4884.997	1	4885	4.06	0.0441	3.84
	Error	1223456.25	1018	1201.82			
	Total	1228341.25	1019				
May 2016 (Rn)	Groups	1407.9	1	1407.9	3.99	0.0462	3.84
	Error	344778	976	353.26			
	Total	346186.5	977				

These methods were (a) unsupervised classification or clustering, (b) supervised classification, (c) index-based methods, and (d) physically-based methods. The results from visual and statistical assessments indicated that the accuracy of the supervised classification method and the index-based method were generally comparable to one another, and superior to the other two. Furthermore, an ANOVA assessment between sunlit or shaded canopy indicates statistical differences between the two groups for both NDVI and LAI estimates. Finally, the impacts of shadows on ET estimation and other fluxes using energy balance models and high-resolution RS data is shown to be significant. According to the TSEB output, G increased, Rn, H, and available energy (Rn-G) decreased in involving shadows scenario. However in most cases the overall effect on LE was minimal, although in certain areas in the vineyard differences were significant. This implies that high-resolution models of ET and biophysical parameters should consider the impact of shadowed areas that could cause significant bias in ET model results in selected areas within a vineyard. The analyses presented, together with the emerging ability to employ UAV-based RS technologies to acquire high-resolution, scientific-grade spectral data in three dimensions, (high-resolution DTM and DSM data, and point cloud data), also point to the possibility of successfully applying high-resolution energy balance modeling techniques to acquire plant-scale estimates of ET and plant stress. Such information could be potentially exploited by growers to manage irrigation deliveries in differential patterns within individual fields while, at the same time, conserving water and reducing management costs. Additional research is required to prove this capability has utility and economic return for high-

value crops, such as wine grapes. Future steps based on this work involve the diurnal modeling of shadows for quantification of their impact on energy balance model results, as well as incorporation of shadow conditions into energy balance models algorithms.

Acknowledgements This project was financially supported under Cooperative Agreement No. 58-8042-7-006 from the U.S. Department of Agriculture and by the Utah Water Research Laboratory at Utah State University. The authors wish to thank E&J Gallo Winery for their continued collaborative support of this research, and the AggieAir UAV Remote Sensing Group at the Utah Water Research Laboratory for their UAV technology and skill and hard work in acquiring the scientific quality, high-resolution aerial imagery used in this project.

Conflict of interest On behalf of all authors, the corresponding author states that there is no conflict of interest.

References

1. AgiSoft, L. L. C., and Russia St Petersburg. "Agisoft photoscan." Professional Edition (2016).
2. Anderson, M. C., Neale, C. M. U., Li, F., Norman, J. M., Kustas, W. P., Jayanthi, H., and Chavez, J. (2004). Upscaling ground observations of vegetation water content, canopy height, and leaf area index during SMEX02 using aircraft and Landsat imagery. Remote Sensing of Environment, 92, 447-464.
3. Bethsda, M. D. (1997). Manual of Photographic Interpretation. 2nd edition, American Society Photogrammetry and remote sensing (ASPRS).
4. Congalton, R.G. (1991). A review of assessing the accuracy of classifications of remotely sensed data. Remote Sensing of Environment, 37(1), 35-46.
5. Campbell, G. S. and Norman, J. M. (1998). An introduction to environmental biophysics, Springer-Verlag, New York.
6. Carlson, T. N., and Ripley, D. A. (1997). On the relation between NDVI, fractional vegetation cover, and leaf area index. Remote Sensing of Environment, 62(3), 241-252.
7. Choi, H., and Bindschadler, R. (2004). Cloud detection in Landsat imagery of ice sheets using shadow matching technique and automatic normalized difference snow index threshold value decision. Remote Sensing of Environment, 91(2), 237-242.
8. Elarab, M., Ticlavilca, A.M., Torres-Rua, A.F., Maslova, I., and McKee, M (2015). Estimating chlorophyll with thermal and broadband multispectral high resolution imagery from an unmanned aerial system using relevance vector machines for precision agriculture. International Journal of Applied Earth Observation and Geoinformation. 43, 32-42.
9. Fuentes, S., Poblete-Echeverra, C., Ortega-Farias, S., Tyerman, S., and De Bei, R. (2014). Automated estimation of leaf area index from grapevine canopies using cover photography video and computational analysis methods. Australian Journal of Grape Wine Research. 20(3), 465-473.
10. Gonzalez, R.C., Woods, R.E., and Eddins, S.L. (2004). Digital Image Processing Using MATLAB., Prentice Hall.
11. Huang, J., and Chen, C. (2009a). A physical approach to moving cast shadow detection. IEEE International Conference on Acoustics, Speech and Signal Processing, 769-772.
12. Huang, J., and Chen, C. (2009b). Moving cast shadow detection using physics-based features. IEEE Conference on Computer Vision and Pattern Recognition, 2310-2317.
13. Kiran, T. S. (2016). A framework in shadow detection and compensation of images. DJ Journal of Advances in Electronics and Communication Engineering, 2(3), 1-9.
14. Kumar, P., Sengupta, K., Lee, A. (2002). A comparative study of different color spaces for foreground and shadow detection for traffic monitoring system. The IEEE 5th International Conference on Intelligent Transportation Systems, 100105.
15. Leblon, B., Gallant, L., and Charland, S. D. (1996a). Shadowing effects on SPOT-HRV and high spectral resolution reflectance in Christmas tree plantation. International of Journal of Remote Sensing, 17(2), 277-289.
16. Leblon, B., Gallant, L., and Grandberg, H. (1996b). Effects of shadowing types on ground-measured visible and near-infrared shadow reflectance. Remote Sensing of Environment, 58 (3), 322328.
17. Lillesand, T. M., and Kiefer, R. W. (2000). Remote Sensing and Image Interpretation. 4th edition. New York, Wiley.
18. http://www.technologyreview.com/lists/technologies/2014/
19. Cook, B. D., L. W. Corp, R. F. Nelson, E. M. Middleton, D. C. Morton, J. T. McCorkel, J. G. Masek, K. J. Ranson, V. Ly, and P. M. Montesano. (2013). NASA Goddard's Lidar, Hyperspectral and Thermal (G-LiHT) airborne imager. Remote Sensing 5:4045-4066, doi:10.3390/rs5084045
20. Nemani, R. R., and Running, S. W. (1989). Estimation of regional surface resistance to evapotranspiration from NDVI and thermal IR AVHRR data. Journal of Applied Meteorology, 28(4), 276-284.

21. Nieto, H., Kustas, W., Torres-Rua, A., Alfieri, J., Gao, F., Anderson, M., White, W. A., Song, L., Mar Alsina, M., Prueger, J., McKee, M., Elarab, M., and McKee, L. (2017). Evaluation of TSEB turbulent fluxes using different methods for the retrieval of soil and canopy component temperatures from UAV thermal and multispectral imagery. Irrigation Science, In press.
22. Norman, J. M., Kustas, W. P., and Humes, K. S. (1995). Source approach for estimating soil and vegetation energy fluxes in observations of directional radiometric surface temperature. Agricultural and Forest Meteorology., 77, 263-293.
23. Ortega-Farias, S., Ortega-Salazar, S., Poblete, T., Kilic, A., Allen, R., Poblete-Echeverra, C., Ahumada-Orellana, L.,Zuiga, M., and Seplveda, D. (2016) Estimation of energy balance components over a drip-irrigated olive orchard using thermal and multispectral cameras placed on a helicopter-based unmanned aerial vehicle (uav), Remote Sensing, 8(8).
24. Qiao, X., Yuan, D, and Li, H. (2017). Urban shadow detection and classification using hyperspectral image. Journal of the Indian Society of Remote Sensing, doi: 10.1007/s12524-016-0649-3.
25. Ranson, K. J., and Daughtry, C. S. T. (1987). Scene shadow effects on multispectral response. IEEE Transactions on Geoscience and Remote Sensing, 25(4), 502-509.
26. Rosin, P.L. and Ellis, T. (1995) Image difference threshold strategies and shadow detection." Proceedings of the 1995 British Conference on Machine Vision,1, 347356.
27. Sandnes, F. E. (2011). Determining the geographical location of image scenes based object shadow lengths. Journal of Signal Processing systems, 65(1), 35-47.
28. Sanin, A., Sanderson, C., and Lovell, B. (2012). Shadow detection: A survey and comparative evaluation of recent methods. Pattern Recognition, 45 (4), 1684-1689.
29. Scanlan, J.M., Chabries, D.M., Christiansen, R., (1990). A shadow detection and removal algorithm for 2-d images. Proceeding IEEE International Conference on Acoustics, Speech, and Signal Processing (ICASSP), 2057-2060.
30. Shiting, W., and Hong, Z. (2013) Clustering-based shadow edge detection in a single color image. International Conference on Mechatronic Sciences, Electric Engineering and Computer (MEC), 1038-1041.
31. Siala, K., Chakchouk, M., Besbes, O., and Chaieb, F. (2004) Moving Shadow Detection with Support Vector Domain Description in the Color Ratios Space. In Proceedings of the 17th IEEE International Conference on Pattern Recognition, pages 384387.
32. Sirmacek, B., and Unsalan, C. (2008). Building detection from aerial images using invariant color features and shadow information. Proceedings of the 23rd International Symposium on Computer and Information Sciences (ISCIS 2008), Istanbul, Turkey, October 27-29, 1-5.
33. Tolt, G., Shimoni, M., and Ahlberg, J., (2011). A shadow detection method for remote sensing images using VHR hyperspectral and LIDAR data. Proceeding. Geoscience and Remote Sensing Symposium, IGARSS, Vancouver Canada, 25-29, July, 4423-4426.
34. Trout, T.J., Johnson, L.F., (2007). Estimating crop water use from remotely sensed NDVI, crop models, and reference ET. USCID Fourth International Conference on Irrigation and Drainage, Sacramento, California October 3-6, 275-285.
35. Xia, H., Chen, X., Guo, P. A. (2009). Shadow detection method for remote sensing images using Affinity Propagation algorithm. In Proceedings of the IEEE International Conference on Systems, Man and Cybernetics, San Antonio, TX, USA, 5-8.
36. Zhu, Z., and Woodcock, C. E. (2012). Object-based cloud and cloud shadow detection in Landsat imagery. Remote Sensing of Environment, 118 (15), 83-94.